Received 31 July 2024; revised 10 November 2024; accepted 17 November 2024. Date of publication 22 November 2024;
date of current version 1 August 2025. The review of this article was arranged by Editor S. Das.

Digital Object Identifier 10.1109/JEDS.2024.3504849

Endurance Enhancement in Hafnia-Based Ferroelectric Capacitor Through Anti-Ferroelectric Zirconia Seed Layer for Memory Applications

MENGXUAN YANG[1], KAIFENG WANG[1] (Graduate Student Member, IEEE), BOCHENG YU[1], ZHIYUAN FU[1], CHANG SU[1], QIANQIAN HUANG[1,2,3] (Member, IEEE), AND RU HUANG[1,2] (Fellow, IEEE)

1 School of Integrated Circuits, Peking University, Beijing 100871, China
2 Beijing Advanced Innovation Center for Integrated Circuits, Beijing 100871, China
3 Beijing Superstring Academy of Memory Technology, Beijing 100176, China

CORRESPONDING AUTHORS: Q. HUANG AND R. HUANG (e-mail: hqq@pku.edu.cn; ruhuang@pku.edu.cn)

This work was supported in part by the National Natural Science Foundation of China (NSFC) under Grant 62374009 and Grant 61927901; in part by the Beijing SAMT Project under Grant SAMT-BD-KT-22030101; in part by the 111 Project under Grant B18001; and in part by the New Cornerstone Science Foundation through the Xplore Prize.

(Mengxuan Yang and Kaifeng Wang contributed equally to this work.)

ABSTRACT In this work, the ferroelectric (FE) $Hf_{0.5}Zr_{0.5}O_2$ (HZO) capacitor with a novel anti-ferroelectric (AFE) ZrO_2 seed layer is thoroughly investigated for memory applications, by comparing with both HZO capacitors without seed layer and with O-phase-dominated ZrO_2 seed layer. A fully vacuum-sealed system is used for device fabrication to mitigate the interfacial defects during the material growth process, and the process conditions are carefully optimized. Experimental results demonstrated that the ZrO_2-based seed layer can enhance ferroelectricity of the HZO capacitor, and the T-phase-dominated ZrO_2 seed layer can further largely enhance the endurance to more than 10^9 without ferroelectricity penalty. Detailed analysis are further performed and demonstrated that the enhanced performance is resulted from the significantly suppressed M-phase ratio and oxygen vacancies. The T-phase dominated ZrO_2 seed layer results in only 3.7% M-phase ratio in HZO and 12% reduction of trap charge density compared with conventional FE capacitors. Moreover, the slower leakage current growth rate in the interface also helps the endurance improvement in the proposed design, indicating its great potential for high reliable FeRAM application.

INDEX TERMS FeRAM, HZO and ZrO_2.

I. INTRODUCTION

The rapid development of Artificial Intelligent of Things (AIoT) applications are driving a lot of memory device innovations for data storage and computing with limited battery capacity and energy-harvesting power supply. Among all kinds of emerging non-volatile memories (NVMs), ferroelectric RAM (FeRAM) has the advantages of ultra-low write energy due to its field-driven operation [1], [2], which is very suitable for AIoT applications. Moreover, the HfO_2-based ferroelectric (FE) material has attracted a lot of attention due to its high CMOS process compatibility, easy integration and good scalability [3]. However, for FeRAM, compared with traditional perovskites-based FE capacitor, HfO_2-based FE capacitor suffers from relatively poor endurance [4] due to its relatively high coercive electric field (E_C) close to the breakdown electric field and high concentration of oxygen vacancies (V_O) which may lead to relatively large leakage currents (I_{leak}) accelerating the breakdown process [5], [6], [7].

So far, many approaches have already been proposed to reduce E_C, V_O and I_{leak} for endurance improvement of HfO_2-based FE capacitor, but always with the penalty of

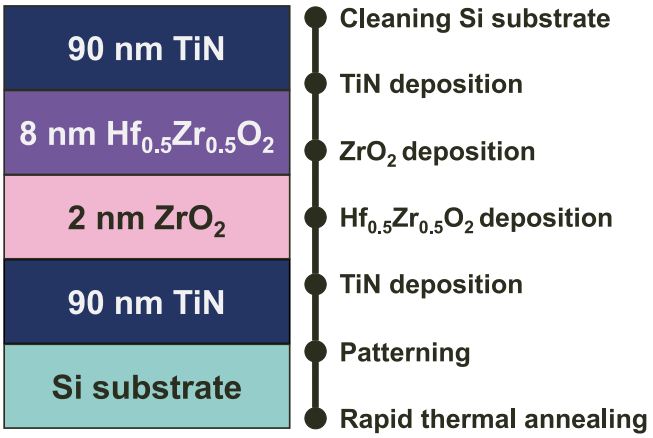

FIGURE 1. **The structure and fabrication process of the proposed AFE-ZrO_2-inserted HZO capacitor.**

remanent FE polarization (P_r). For example, by introducing La into $Hf_{0.5}Zr_{0.5}O_2$ (HZO) can reduce E_C and thus improve the endurance [8], while the high endurance results were accompanied by the low operation electric field and the FE polarization was not saturated. Introducing the Al_2O_3 interlayer into HZO FE capacitor to control grain size can reduce the leakage current and enhance endurance [9], while the P_r degrades rapidly after only 10^5 cycles. Moreover, altering the electrode material can also modulate the leakage current, thereby improving endurance [10], [11], [12], [13]. Ruthenium is utilized as the electrode material to reduce the defect density in HZO and the leakage current was largely reduced, while the endurance at the large electric field for saturated polarization still needs to be optimized [10].

In this work, the endurance of HfO_2-based FE capacitor is improved without the ferroelectricity penalty by introducing a T-phase-dominated ZrO_2 seed layer. The device design and fabrication is discussed in Section II. The enhanced ferroelectricity and endurance are verified in Section III. The roles of T-phase-dominated ZrO_2 seed layer in ferroelectricity and endurance enhancement are further analyzed in Section IV. The proposed FE capacitor with T-phase-dominated ZrO_2 seed layer can optimize the metal/ferroelectric interface to the improve endurance and stabilize the ferroelectric phase of HZO for P_r improvement at the same time.

II. DEVICE DESIGN AND FABRICATION

In previous work, ZrO_2 has been demonstrated as a decent seed layer to enhance the ferroelectricity in thick HZO capacitor [14] and improve the endurance of HZO-based Ferroelectric FET (FeFET) [15]. In this work, for FeRAM, we insert a well-designed T-phase-dominated ZrO_2 (AFE-ZrO_2) layer between thin HZO and bottom electrode to enhance the endurance of FE capacitor, as well as the ferroelectricity.

A. FABRICATION PROCESS

The device structure and fabrication process are shown in Fig. 1. Based on the p-type Si substrate, 90nm titanium nitride (TiN) is magnetron sputtered under 250°C to obtain bottom electrode with dense metal film and low resistivity. The 8nm $Hf_{0.5}Zr_{0.5}O_2$ and 2nm ZrO_2 films are deposited by thermally oxidized atomic layer deposition (ALD) afterwards. The $Hf_{0.5}Zr_{0.5}O_2$ layer of 0.2nm is generated under 300°C through one cycle TEMAH with 50 sccm, one cycle H_2O with 100 sccm, one cycle TEMAZ with 50 sccm and one cycle H_2O with 100 sccm. The ZrO_2 film of 0.1nm is generated under 250°C by one cycle TEMAZ with 50 sccm and one cycle H_2O with 100 sccm. Then another 90nm TiN is magnetron sputtered under 250°C to fabricate top electrode. To mitigate the interfacial defects during the growth process, a fully vacuum-sealed interconnect conduit is employed to connect equipments of above fabrication processes. After all the deposition steps, device samples are then transferred from the vacuum conduit for patterning and annealing processes. The patterning process is fulfilled through photo lithography and ion beam etching (IBE). The rapid thermal annealing is performed to induce the ferroelectricity of FE capacitor.

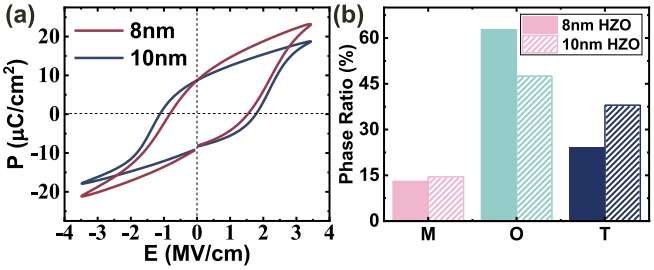

FIGURE 2. **(a) PV curves and (b) phase ratio of TiN/HZO/TiN with different thickness of HZO.**

B. OPTIMIZATION OF THE PROCESS CONDITIONS

Experiments are performed first to obtain the optimal process conditions of FE capacitor. According to [16], ferroelectric capacitor with 8nm HZO demonstrates the largest P_r among different thickness, since the P_r degrades drastically for HZO below 8 nm due to relatively large leakage current and the P_r degrades slowly for HZO above 8nm due to the decreasing O-phase. As shown in our experimental results in Fig. 2, similar with the results in [16], the fabricated 8nm FE-HZO capacitor shows better ferroelectricity properties than 10nm FE-HZO capacitors. As for the electrode, the TiN electrode with low resistivity can improve the ferroelectricity of HZO [17], and the resistivity of TiN will decrease with the higher deposition temperature [18]. Fig. 3 demonstrates that TiN deposited under 250°C can result in the larger P_r and the smaller E_c on both 8nm and 10nm FE-HZO capacitors than TiN deposited under 200°C in our experiments.

Since the annealing conditions will significantly influence the crystallization of the HZO material for the orthogonal phase and thereby affect the ferroelectricity [16], in this experimental work, six RTA conditions are performed to obtain the optimal annealing conditions. As shown in Fig. 4 of the GIXRD results, the test spectral line data were further analyzed using Gaussian distribution fitting to extract the

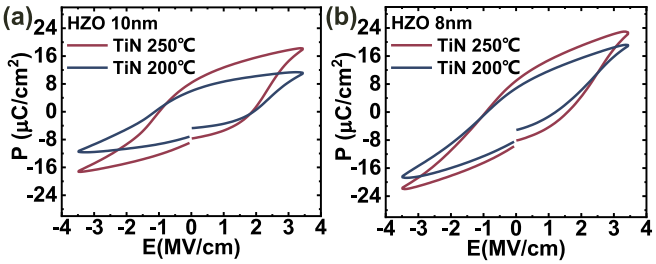

FIGURE 3. Comparison of PV curves of TiN/HZO/TiN capacitors with different TiN growth temperatures. (a) 10nm HZO capacitor. (b) 8nm HZO capacitor.

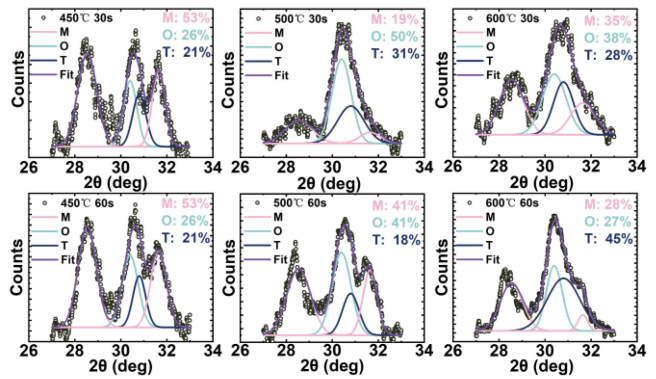

FIGURE 4. The Gaussian fitting results of the GIXRD spectral line data for the HZO ferroelectric peak near 30.5° under different annealing conditions.

proportion of each crystal phase in the HZO ferroelectric layer [16]. The lower temperature cannot provide enough thermal budget for the HZO layer to crystallize into the orthogonal phase. Too high annealing temperature and longer annealing time will increase the M phase ratio [19]. Therefore, 500°C 30s is selected as the optimal annealing condition.

Moreover, as for the material deposition temperature, the ZrO_2 will change from T-phase to O-phase when the deposition temperature is too high [20]. In this work, as shown in Fig. 5, the ZrO_2 film is dominated by T-phase at 250°C deposition temperature and shows a typical anti-ferroelectric (AFE) PV hysteresis curve. The thickness of AFE-ZrO_2 is further optimized and the 2nm AFE-ZrO_2 is selected due to the largest P_r and the smallest E_c for the proposed FE capacitor design. STEM results in our previous work [21] have verified that the 2nm ZrO_2 seed layer deposited at 250°C is T-phase-dominated and the 2nm ZrO_2 seed layer deposited at 300°C is O-phase-dominated in TiN/ZrO_2/HZO/TiN capacitors.

III. RESULTS AND DISCUSSION

Based on the above process condition, the fabricated 8nm FE-HZO capacitor with 2nm AFE-ZrO_2 seed layer is systematically characterized and compared with 8nm FE-HZO capacitors without seed layer and with 2nm FE-ZrO_2 seed layer, respectively.

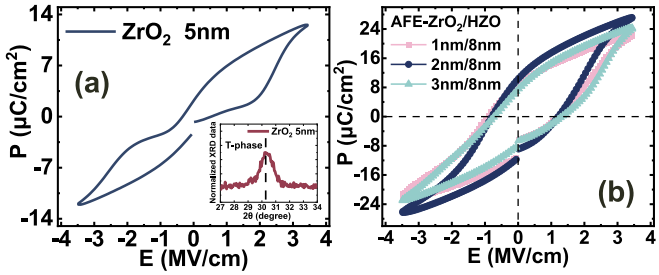

FIGURE 5. (a) Normalized XRD data and PV curves of AFE-ZrO_2 capacitors with ZrO_2 deposited at 250°C. (b) PV curves of AFE-ZrO_2/HZO capacitors with different thickness of ZrO_2.

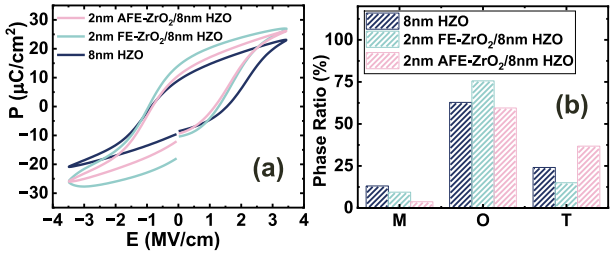

FIGURE 6. (a) PV curves and (b) phase ratio of HZO, FE-ZrO_2/HZO and AFE-ZrO_2/HZO capacitors.

A. FERROELECTRICITY

As shown in Fig. 6, both the FE-ZrO_2 layer and the AFE-ZrO_2 layer can increase P_r and reduce E_c for HZO capacitor as seed layer due to the higher (O+T) phase ratio while the M phase ratio is significantly lower, which verified that the crystallized ZrO_2 can promote the transition of the M phase to the O/T phase for higher P_r [22], [23].

To further obtain the measurement conditions of electric field (E_{FE}) and pulse width (T_{FE}) for saturated polarization switching, the "write and read" operation method is utilized to extract the switched ferroelectric polarization (P_{SW}) as demonstrated in Fig. 7. A negative pulse is first applied to write "1" like in the FeRAM application. Then, three positive pulses are applied to read "1", write "0" and read "0". Current during each reading operation are accumulated to calculate the amount of polarization switching, and the P_{SW} is obtained by subtracting the amount of polarization switching from two reading operations. With increasing E_{FE} and T_{FE}, P_{SW} gradually gets saturated. All three kinds of capacitors achieve saturated polarization switching at 3.5MV/cm and 10μs, which are then selected as the pulse conditions for endurance measurement. Meanwhile, it is noted that the capacitor without seed layer also shows the lowest saturated P_{SW}, demonstrating the superior effect of the seed layer on enhancing ferroelectricity.

B. ENDURANCE

The endurance is measured with PUND approach with 3.5MV/cm electric field and 10μs pulse width to ensure saturated polarization switching. As shown in Fig. 8, the

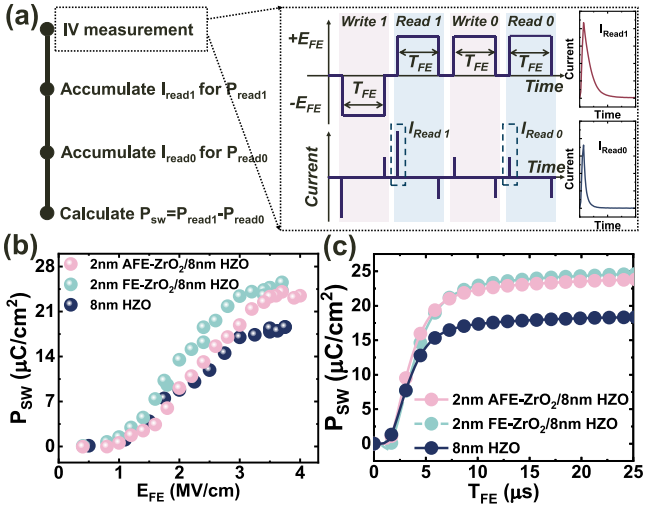

FIGURE 7. (a) Methods to extract the switched ferroelectric polarization P_{SW}. P_{SW} of three kinds of ferroelectric capacitors under (b) different maximum electric field E_{FE} and (c) different pulse width T_{FE}.

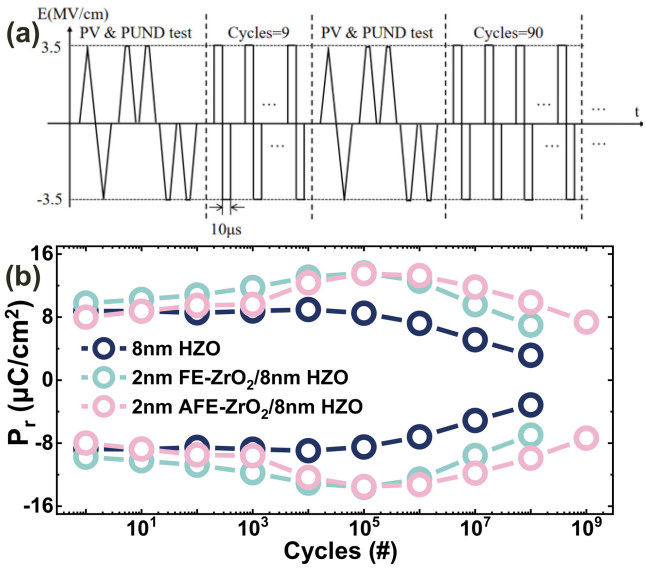

FIGURE 8. (a) The input voltage pulse sequence of the cycling test with PUND. (b) Endurance of three kinds of capacitors.

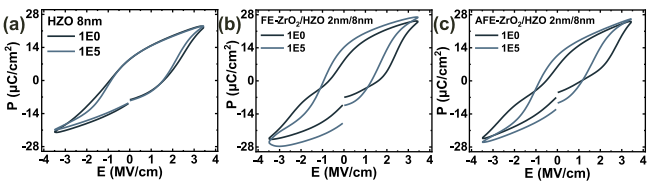

FIGURE 9. PV curves before and after wakeup of three different structures.

measurement results show that the endurance of TiN/AFE-ZrO_2/HZO/TiN capacitor can be improved by more than one order of magnitude, and the highest P_r after wake-up is also obtained. Compared with conventional TiN/HZO/TiN, the HZO capacitors with seed layers have distinct wake-up behavior. Fig. 9 shows and compares the PV curves

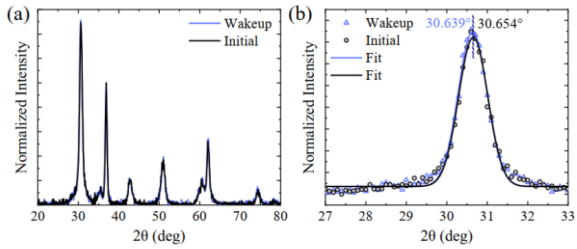

FIGURE 10. XRD results of AFE-ZrO_2/HZO capacitor before and after wakeup.

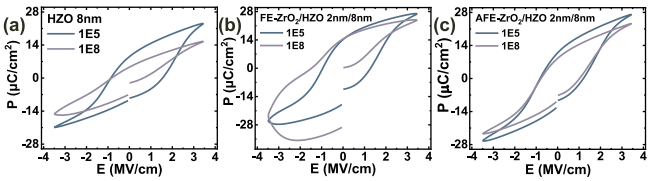

FIGURE 11. PV curves before and after fatigue of three different structures.

before and after wakeup for different ferroelectric capacitors. The conventional TiN/HZO/TiN structure shows almost no difference after 10^5 cycles enabling wake-up free. In contrast, the initial PV curves of the HZO capacitors with seed layers shows anti-ferroelectric-like behavior due to the impact of ZrO_2. To verify the mechanism of wakeup behavior, the X-ray diffraction (XRD) analysis is conducted on the HZO capacitor with AFE-ZrO_2 seed layer before and after wakeup. As depicted in Fig. 10, there is only a slight shift in the GIXRD result after wakeup, suggesting the possibility of the phase transition. However, this shift is too small that the phase transition is not the dominant factor for the wakeup behavior. Therefore, the oxygen vacancy theory is used in this paper.

From Fig. 9 and Fig. 11, it can be seen that the leakage gap increases with cycles increasing. HZO capacitor with AFE-ZrO_2 seed layer has the smallest leakage gap whereas HZO capacitor with FE-ZrO_2 seed layer has the largest one. The ZrO_2-based seed layer can promote the crystallization of HZO, and thus there are more grain boundaries penetrating the two electrodes [22], resulting in an increase in leakage current as the FE-ZrO_2/FE-HZO capacitor demonstrated [23]. However, oxygen vacancy concentration has the greater contribution to the leakage currents and the small leakage current of AFE-ZrO_2/FE-HZO capacitor suggests that it may have low enough oxygen vacancy concentration for the leakage current suppression.

The detailed mechanisms about the leakage current and oxygen vacancies will be analyzed in the following subsections.

C. TRAP ANALYSIS

The conductivity complex analysis [24] is used to extract the traps between the ZrO_2 and TiN for further leakage current analysis in FE-ZrO_2/FE-HZO capacitor and

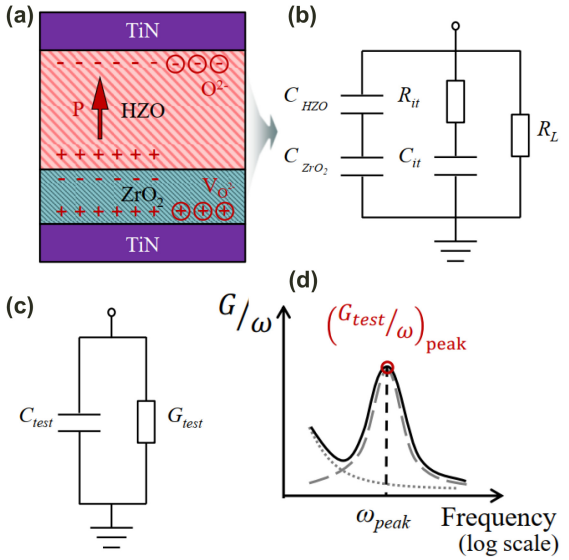

FIGURE 12. Schematics of (a) defects distributions, (b) equivalent circuit model, (c) model of test circuit and (d) measured curves of the proposed device.

AFE-ZrO_2/FE-HZO capacitor. Fig. 12(a) illustrates the ferroelectric switching mechanism and the distribution of defects in the TiN/ZrO_2/HZO/TiN structure. Since the HZO and ZrO_2 deposition process in this experiment is continuous in vacuum-sealed environment and the crystalline structure remains unbroken, the interface between the layers is not considered as the principal region for the aggregation of defect charges. Defect charges are mainly present at the electrode interfaces of the bottom and top TiN layers.

Fig. 12(b) is the schematic of the equivalent circuit model of the proposed device. The FE capacitance C_{HZO} and the AFE capacitance C_{ZrO2} are series connected. The interface charge is described by the series connection of the trap charge capacitance C_{it} and the resistance R_{it}, while the leakage current is described by the impedance R_L. Specifically, R_{it} represents the loss process of the trapping charges, and the trap capacitance is given by $C_{it} = qD_{it}$, where D_{it} is the interface trap charge density per unit electron energy. The CV-GF testing module of the 4200 semiconductor parameter analyzer is used for this analysis and the equivalent model of the test circuit is shown in Fig. 12(c). The relationship between C_{test} and G_{test} in Fig. 9(c) with the components in Fig. 9(b) can be derived as equation (1) and (2).

$$C_{test} = \frac{C_{HZO}C_{ZrO2}}{C_{HZO} + C_{ZrO2}} + \frac{C_{it}}{w^2 C_{it}^2 R_{it}^2 + 1} \tag{1}$$

$$G_{test}/w = 1/R_L w + \frac{wC_{it}^2 R_{it}}{w^2 C_{it}^2 R_{it}^2 + 1} \tag{2}$$

Both the first and second terms of the equation (2) include a frequency component. The magnitude of the first term in equation (2) is inversely proportional to the frequency. And its relationship corresponds to the monotonically decreasing dashed line in the G_{test}/w-Frequency plot of Fig. 12(d). This term predominates at low frequencies but can be neglected at high frequencies. The second term of equation (2) has both the numerator and the denominator containing frequency terms, and their relationship corresponds to the parabolic dashed line in the G_{test}/w-Frequency plot of Fig. 12(d). This term tends towards zero when the frequency w is zero or infinitely large, with a peak value existing. The derivative of G_{test}/w equal to zero can yield this peak value. In the high-frequency stage, the derivative of G_{test}/w can be simplified to the derivative of the second term, which allows for the determination of the peak value. The results can be represented by equation (3) and (4).

$$w_{peak} = 1/R_{it}C_{it} \tag{3}$$

$$(G/w)_{peak} = C_{it}/2 \tag{4}$$

It is evident that the peak value of G_{test}/w, denoted as $(G/w)_{peak}$, is equal to $C_{it}/2$. The larger the peak value, the greater the value of C_{it}, which implies a larger interface trap charge density per unit electron energy, D_{it}.

Fig. 13 demonstrates the experimental results. It can be seen that the interface trap charge density of the TiN/AFE-ZrO_2/HZO/TiN is about 12% lower than that of TiN/FE-ZrO_2/HZO/TiN under the same voltage bias. Therefore, it is verified that increasing the T-phase proportion in ZrO_2 seed layer can reduce the interface trap charge density and thus reduce the leakage current and the growth rate of oxygen vacancies during electrical cycling.

D. LEAKAGE CURRENT ANALYSES

From the electrical cycling PV test diagrams in Fig. 9 and Fig. 11, it can be observed that as the number of cycles increases, the leakage current gap in the PV test curves becomes progressively larger. Therefore, the leakage current variation are further studied to reflect the variation in oxygen vacancy concentration throughout the entire electrical cycling process. Fig. 14 shows the schematic diagram of leakage current extraction method. The black lines in the diagram represent the two sequential rising and two falling voltage pulses input during the PUND test, while the red lines correspond to the four output current curves. Fig. 14(a) is the current curve corresponding to the first positive up voltage pulse and Fig. 14(b) is the current curve corresponding to the second positive up voltage pulse. When the first positive up voltage pulse is applied, the ferroelectric polarization is completely switching. During the second positive up voltage pulse, there is no further polarization switching, and the corresponding current does not include the current from the positive ferroelectric polarization switching. When this current stabilizes, it represents the remaining leakage current at the positive voltage, and the current at the end of the voltage pulse plateau is the most stable, which is indicated by the black arrow in the diagram. Similarly, Fig. 14(d) is the current curve corresponding to the second negative up voltage pulse, and the negative leakage current is the size of the current indicated by the black arrow.

Following the aforementioned method for extracting leakage current, the leakage current from PUND tests for ferroelectric devices with three different structures in this work are extracted at various cycling numbers as shown in Fig. 15. Firstly, by comparing the conventional TiN/HZO/TiN and TiN/ZrO_2/HZO/TiN structures, it is observed that the leakage current increases after the insertion of FE-ZrO_2 seed layer. It is because that the ZrO_2 seed layer can induce crystallization, resulting in a greater number of grain boundaries spanning the electrodes [25], [26], which leads to an increase in leakage current [27], [28]. Furthermore, by comparing the TiN/HZO/TiN structure with the proposed TiN/AFE-ZrO_2/HZO/TiN structure, it is found that the additional AFE-ZrO_2 seed layer does not significantly increase the leakage current. In the fatigue-to-breakdown region, the TiN/AFE-ZrO_2/HZO/TiN structure can even exhibit a smaller leakage current phenomenon.

To analyze the above phenomenon, the oxygen vacancy concentration are further discussed. Extensive research on the mechanism of leakage current indicates that the magnitude of leakage current in HZO devices is determined by the concentration of oxygen vacancies [6], [29]. The multi-phonon-assisted ionic trap model described by Makram-Ebeid and Lannoo is well consistent with experimental data [6], where the transport equation can be expressed as equation (5).

$$a\nabla\left(n_t\left(1-\frac{n_t}{N}\right)P\right)=\frac{1}{e}\nabla J \tag{5}$$

where a represents the distance between two adjacent traps, n_t is the trap density for charge filling in the area, N is the total trap density in the region, e is the elementary charge, and J is the current density. P denotes the tunneling rate between adjacent traps as described by Nasyrov and Gritsenko. Assuming a uniform distribution of oxygen vacancies to simplify the analysis, a relationship between the leakage current and parameters such as the concentration of oxygen vacancies can be derived as equation (6) and (7).

$$J=eN^{\frac{2}{3}}\frac{n_t}{N}\left(1-\frac{n_t}{N}\right)P \tag{6}$$

$$P=\frac{2\sqrt{\pi}W_t}{m^*a^2Q_0\sqrt{kT}}exp\left(-\frac{W_{opt}-W_t}{2kT}\right)\times exp\left(-\frac{2a\sqrt{2m^*W_t}}{\hbar}\right)sinh\left(\frac{eFa}{2kT}\right) \tag{7}$$

where $\hbar$ is the Planck constant, k is the Boltzmann constant, T is the temperature, m* is the effective mass of the charge carriers, W_{opt} and W_t are the energy levels of the two types of traps, and F is the electric field. The main body of the leakage current formula consists of the terms $N^{2/3}$ and P, with the predominant trend being that an increase in oxygen vacancies leads to an increase in leakage current. Both theory and formula indicate a very direct correspondence between the concentration of oxygen vacancies and leakage current, which is mainly a positive correlation. It is reasonable to assume that during the electrical cycling process, under the same electric field, the comparative relationship of the oxygen vacancies number between different devices is similar to the comparative relationship of leakage current.

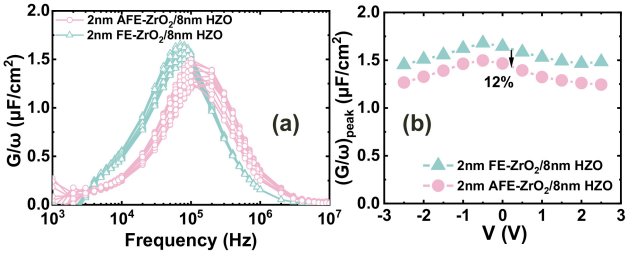

FIGURE 13. Measured Interface defect charge of the fabricated devices.

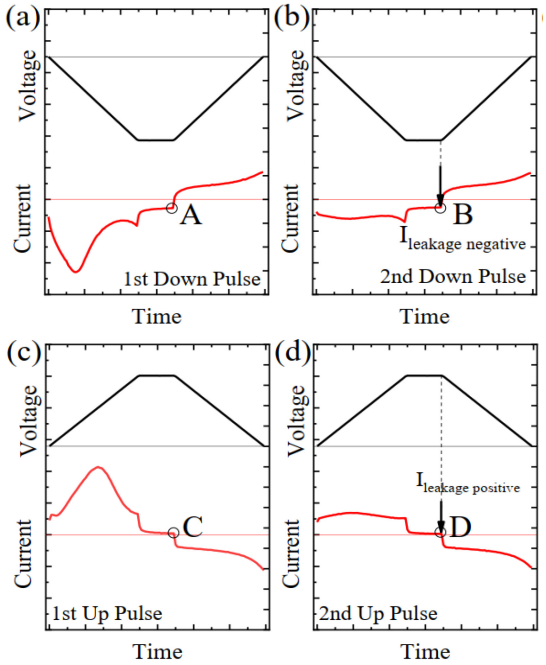

FIGURE 14. Schematic diagram of leakage current extraction method with PUND.

Additionally, the leakage current curves of the HZO FE capacitors with seed layer in Fig. 15 exhibit a phased peak at around 10^5 cycles. As shown in equation (6), there is a quadratic term in the formula that includes $\frac{n_t}{N}(1-\frac{n_t}{N})$ and reaches its maximum value when $n_t = 0.5N$, which makes it possible for the leakage current to have a regional maximum value during the process of increasing oxygen vacancy concentration. The formula's coefficient and exponent terms contain parameters of defect spacing or oxygen vacancy concentration in many places, and the concentration of oxygen vacancies is not uniform in practical situations. The relationship between actual leakage current and oxygen vacancy concentration will be more complex, and the change in leakage current has a certain degree of randomness [30], [31]. Therefore, it is concluded that compared with the TiN/ZrO_2/HZO/TiN structure, the proposed TiN/AFE-ZrO_2/HZO/TiN structure

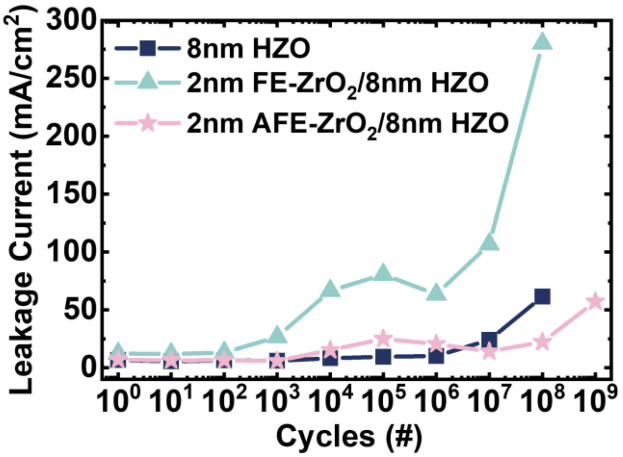

FIGURE 15. Measured leakage current magnitude in ferroelectric devices with three different structures: TiN/HZO/TiN, TiN/ZrO_2/HZO/TiN, and TiN/AFE-ZrO_2/HZO/TiN, under different cycling numbers.

has the significantly lower concentration of oxygen vacancies under the same electrical cycles, and the leakage current begins to increase later, indicating that the increase rate in leakage current during the electrical cycling measurement is slower. Compared with the conventional HZO ferroelectric capacitors, the proposed AFE ZrO_2 seed layer enables the lower leakage current in the fatigue-breakdown region, reflecting that it also has a lower growth rate of oxygen vacancies compared with HZO.

IV. CONCLUSION

A novel HZO ferroelectric capacitor with T-phase-dominated AFE-ZrO_2 as seed layer is proposed to solve the problem of "P_r-endurance dilemma" for ferroelectric memory. It is experimentally verified that the proposed capacitor design can largely improve the endurance while ensuring high P_r compared with conventional HZO capacitors and FE-ZrO_2/FE-HZO capacitors. The extremely low M phase ratio (3.7%) in HZO, the lower trap charge density (about 12% reduction) and the slower leakage current growth rate in the interface are extracted, showing the great potential of AFE-ZrO_2/HZO capacitor for highly reliable FeRAM applications.

ACKNOWLEDGMENT

The authors are thankful to NANO-X Vacuum Interconnected Nanotech Workstation in SINANO, CAS for the support during device fabrication.

REFERENCES

[1] J. U. Duncombe, "Infrared navigation—Part I: An assessment of feasibility," *IEEE Trans. Electron Devices*, vol. 11, no. 1, pp. 34–39, Jan. 1959, doi: 10.1109/TED.2016.2628402.
[2] B.-G. Jeon et al., "A 0.4-/spl mu/m 3.3-V 1T1C 4-Mb nonvolatile ferroelectric RAM with fixed bitline reference voltage scheme and data protection circuit," *IEEE J. Solid-State Circuits*, vol. 35, no. 11, pp. 1690–1694, Nov. 2000.
[3] S. Khanna et al., "17.4 16MHz FRAM micro-controller with a low-cost sub-1μA embedded piezo-electric strain sensor for ULP motion detection," in *Proc. IEEE Int. Solid-State Circuits Conf. (ISSCC)*, San Francisco, CA, USA, 2019, pp. 282–284.
[4] M. Sung et al., "Low voltage and high speed 1Xnm 1T1C FE-RAM with ultra-thin 5nm HZO," in *Proc. IEEE Int. Electron Devices Meeting (IEDM)*, San Francisco, CA, USA, 2021, pp. 33.3.1–33.3.4.
[5] M. H. Park, Y. H. Lee, T. Mikolajick, U. Schroeder, and C. S. Hwang, "Review and perspective on ferroelectric HfO_2-based thin films for memory applications," *Mrs Commun.*, vol. 8, no. 3, pp. 795–808, 2018.
[6] D. R. Islamov et al., "Identification of the nature of traps involved in the field cycling of $Hf_{0.5}Zr_{0.5}O_2$-based ferroelectric thin films," *Acta Materialia*, vol. 166, pp. 47–55, Mar. 2019.
[7] D. R. Islamov, T. M. Zalyalov, O. M. Orlov, V. A. Gritsenko, and G. Y. Krasnikov, "Impact of oxygen vacancy on the ferroelectric properties of lanthanum-doped hafnium oxide," *Appl. Phys. Lett.*, vol. 117, no. 16, 2020, Art. no. 162901.
[8] A. G. Chernikova et al., "Improved ferroelectric switching endurance of La -doped $Hf_{0.5}Zr_{0.5}O_2$ thin films," *ACS Appl. Mater. Interfaces*, vol. 10, no. 3, pp. 2701–2708, 2018.
[9] Y. Xu et al., "Robust breakdown reliability and improved endurance in $Hf_{0.5}Zr_{0.5}O_2$ ferroelectric using grain boundary interruption," *IEEE Trans. Electron Devices*, vol. 69, no. 1, pp. 430–433, Jan. 2022.
[10] R. Cao et al., "Improvement of endurance in HZO-based ferroelectric capacitor using Ru electrode," *IEEE Electron Device Lett.*, vol. 40, no. 11, pp. 1744–1747, Nov. 2019.
[11] G. Karbasian, R. Dos Reis, A. K. Yadav, A. J. Tan, C. Hu, and S. Salahuddin, "Stabilization of ferroelectric phase in tungsten capped $Hf_{0.8}Zr_{0.2}O_2$," *Appl. Phys. Lett.*, vol. 111, no. 2, 2017, Art. no. 22907.
[12] R. Cao et al., "Effects of capping electrode on ferroelectric properties of $Hf_{0.5}Zr_{0.5}O_2$ thin films," *IEEE Electron Device Lett.*, vol. 39, no. 8, pp. 1207–1210, Aug. 2018.
[13] Y. Goh and S. Jeon, "The effect of the bottom electrode on ferroelectric tunnel junctions based on CMOS-compatible HfO_2," *Nanotechnology*, vol. 29, no. 33, 2018, Art. no. 335201
[14] T. Onaya et al., "Improvement in ferroelectricity of $Hf_xZr_{1-x}O_2$ thin films using ZrO2 seed layer," *Appl. Phys. Express*, vol. 10, no. 8, 2017, Art. no. 81501.
[15] W. Xiao et al., "Memory window and endurance improvement of $Hf_{0.5}Zr_{0.5}O_2$-Based FeFETs with ZrO_2 seed layers characterized by fast voltage pulse measurements," *Nanoscale Res. Lett.*, vol. 14, p. 254, Jul. 2019.
[16] S. J. Kim et al., "Effect of film thickness on the ferroelectric and dielectric properties of low-temperature (400 °C) $Hf_{0.5}Zr_{0.5}O_2$ films," *Appl. Phys. Lett.*, vol. 112, no. 17, 2018, Art. no. 172902.
[17] R. Fuji, M. Ishimaru, S. Migita, and N. Uchida, "Structure analysis of $Hf_{0.5}Zr_{0.5}O_2$ Thin Films Crystallized from Amorphous Phase by Thermal Annealing below 500°C," in *Proc. Silicon Nanoelectron. Workshop (SNW)*, Kyoto, Japan, 2021, pp. 1–2.
[18] L. Cui, W. Zhang, and J. Che, "Effect of electrode on dielectric susceptibility and pyroelectric properties of a ferroelectric thin film capacitor using Landau-Khalatnikov theory," *Chin. J. Phys.*, vol. 68, pp. 461–467, Dec. 2020.
[19] M. Hyuk Park, H. Joon Kim, Y. Jin Kim, W. Lee, T. Moon, and C. S. Hwang, "Evolution of phases and ferroelectric properties of thin $Hf_{0.5}Zr_{0.5}O_2$ films according to the thickness and annealing temperature," *Appl. Phys. Lett.*, vol. 102, no. 24, 2013, Art. no. 242905.
[20] F. Magnus, A. S. Ingason, S. Olafsson, and J. T. Gudmundsson, "Nucleation and resistivity of ultrathin TiN films grown by high-power impulse magnetron sputtering," *IEEE Electron Device Lett.*, vol. 33, no. 7, pp. 1045–1047, Jul. 2012.
[21] M. Yang et al., "A novel hafnia-based ferroelectric capacitor with antiferroelectric zirconia seed layer for high ferroelectricity and endurance," in *Proc. 8th IEEE Electron Devices Technol. Manuf. Conf. (EDTM)*, 2024, pp. 1–3.
[22] S. Shibayama, T. Nishimura, S. Migita, and A. Toriumi, "Thermodynamic control of ferroelectric-phase formation in $HfxZr_{1-x}O_2$ and ZrO2," *J. Appl. Phys.*, vol. 124, no. 18, 2018, Art. no. 184101.
[23] T. Onaya et al., "Improvement in ferroelectricity of $HfxZr_{1-x}O_2$ thin films using ZrO_2 seed layer," *Appl. Phys. Exp.*, vol. 10, no. 8, Art. no. 81501, 2017.
[24] G. Lucovsky, C. L. Hinkle, C. C. Fulton, N. A. Stoute, H. Seo, and J. Lüning, "Intrinsic nanocrystalline grain-boundary and oxygen atom vacancy defects in ZrO_2 and HfO_2," *Radiat. Phys. Chem.*, vol. 75, no. 11, pp. 2097–2101, 2006.

[25] T. Onaya et al., "Improvement in ferroelectricity of HfxZr$_{1-x}$O$_2$ thin films using ZrO$_2$ seed layer," *Appl. Phys. Express*, vol. 10, no. 8, 2017, Art. no. 81501.
[26] R. Koduru, A. K. Saha, M. Si, X. Lyu, P. D. Ye, and S. K. Gupta, "Variation and stochasticity in polycrystalline HZO based MFIM: Grain-growth coupled 3D phase field model based analysis," in *Proc. IEEE Int. Electron Devices Meeting (IEDM)*, 2021, pp. 15.2.1–15.2.4.
[27] G. Bersuker et al., "Grain boundary-driven leakage path formation in HfO$_2$ dielectrics," *Solid-State Electron.*, vols. 65–66, pp. 146–150, Nov./Dec. 2011.
[28] B. Y. Kim et al., "Study of ferroelectric characteristics of Hf$_{0.5}$Zr$_{0.5}$O$_2$ thin films grown on sputtered or atomic-layer-deposited TiN bottom electrodes," *Appl. Phys. Lett.*, vol. 117, no. 2, 2020, Art. no. 22902.
[29] D. R. Islamov et al., "Leakage currents mechanism in thin films of ferroelectric Hf$_{0.5}$Zr$_{0.5}$O$_2$," *ECS Trans.*, vol. 75, no. 32, p. 123, 2017.
[30] W. C. Chen et al., "Investigation on the current conduction mechanism of HfZrOx ferroelectric memory," *J. Phys. D, Appl. Phys.*, vol. 53, no. 44, 2020, Art. no. 445110.
[31] Z. Wu and J. Zhu, "Enhanced unipolar resistive switching characteristics of Hf$_{0.5}$Zr$_{0.5}$O$_2$ thin films with high ON/OFF ratio," *Materials*, vol. 10, no. 3, p. 322, 2017.